Water Resources Research

RESEARCH ARTICLE
10.1029/2019WR025517

Adjustment of Radar-Gauge Rainfall Discrepancy Due to Raindrop Drift and Evaporation Using the Weather Research and Forecasting Model and Dual-Polarization Radar

Qiang Dai[1,2,3], Qiqi Yang[1,2], Dawei Han[2], Miguel A. Rico-Ramirez[2], and Shuliang Zhang[1]

[1]Key Laboratory of VGE of Ministry of Education, Nanjing Normal University, Nanjing, China, [2]Department of Civil Engineering, University of Bristol, Bristol, UK, [3]Jiangsu Center for Collaborative Innovation in Geographical Information Resource Development and Application, Nanjing, China

Key Points:
- The impact of raindrop drift and evaporation on radar-gauge rainfall comparison was studied
- The proposed scheme considers both variables and can reduce this discrepancy by as much as 21.7%
- The three-dimensional atmospheric fields downscaled by the WRF can effectively simulate raindrop evolution

Correspondence to:
Q. Dai and S. Zhang,
qd_gis@163.com;
zhangshuliang@njnu.edu.cn

Citation:
Dai, Q., Yang, Q., Han, D., Rico-Ramirez, M. A., & Zhang, S. (2019). Adjustment of radar-gauge rainfall discrepancy due to raindrop drift and evaporation using the Weather Research and Forecasting model and dual-polarization radar. *Water Resources Research*, *55*, 9211–9233. https://doi.org/10.1029/2019WR025517

Received 17 MAY 2019
Accepted 30 OCT 2019
Accepted article online 8 NOV 2019
Published online 16 NOV 2019

Abstract Radar-gauge rainfall discrepancies are considered to originate from radar rainfall measurements while ignoring the fact that radar observes rain aloft while a rain gauge measures rainfall on the ground. Observations of raindrops observed aloft by weather radars consider that raindrops fall vertically to the ground without changing in size. This premise obviously does not stand because raindrop location changes due to wind drift and raindrop size changes due to evaporation. However, both effects are usually ignored. This study proposes a fully formulated scheme to numerically simulate both raindrop drift and evaporation in the air and reduces the uncertainties of radar rainfall estimation. The Weather Research and Forecasting model is used to simulate high-resolution three-dimensional atmospheric fields. A dual-polarization radar retrieves the raindrop size distribution for each radar pixel. Three schemes are designed and implemented using the Hameldon Hill radar in Lancashire, England. The first considers only raindrop drift, the second considers only evaporation, and the last considers both aspects. Results show that wind advection can cause a large drift for small raindrops. Considerable loss of rainfall is observed due to raindrop evaporation. Overall, the three schemes improve the radar-gauge correlation by 3.2%, 2.9%, and 3.8% and reduce their discrepancy by 17.9%, 8.6%, and 21.7%, respectively, over eight selected events. This study contributes to the improvement of quantitative precipitation estimation from radar polarimetry and allows a better understanding of precipitation processes.

1. Introduction

Modern weather radars enable instantaneous precipitation estimation with large areal coverage (e.g., a radius of 200 km) at spatial and temporal resolution as high as 1 km and 5 min. Thus, they have been widely applied in hydrology and meteorology. However, due to the indirect and remotely based observation of hydrometers in a fluctuating atmospheric environment, radar rainfall estimates are subject to large uncertainties. Widely recognized radar rainfall measurement errors include ground clutter and anomalous propagation, signal attenuation, beam blockage, Z-R relation parameterization, and vertical variability in measured radar reflectivity (Bringi & Chandrasekar, 2001; Frasier et al., 2013; Kurri & Huuskonen, 2008; Lang et al., 2009). Physical-based adjustments of these errors are processed step by step using different radar quality control algorithms (Bringi & Chandrasekar, 2001; Villarini & Krajewski, 2010). To obtain a more reliable radar rainfall product, it is necessary to carry out additional statistical adjustments of radar rainfall by leveraging the strengths of rain gauge measurements, which is regarded as the "ground truth" for radar rainfall estimates (Bringi et al., 2011; Dai et al., 2015; Hasan et al., 2016; Villarini et al., 2014). Radar-gauge pairs are constructed at the same time and location (on the ground). Their discrepancies are interpreted as radar rainfall uncertainties and are further partitioned into different error types, such as overall bias, local bias, conditional bias, and random error in various studies (AghaKouchak et al., 2010; Ciach et al., 2007; Germann et al., 2009; Habib et al., 2008; Nerini et al., 2017; Thorndahl et al., 2014). This is widely accepted as an easily implemented and highly effective approach (Dai et al., 2014).

In radar-gauge rainfall comparisons, the discrepancy is considered to originate from the radar rainfall measurement, ignoring the fact that the radar observes the rain regime aloft while the rain gauge captures the

raindrops on the ground (Frasier et al., 2013; Kurri & Huuskonen, 2008). The radar rainfall is directly used as the ground rainfall by a simple projected transform, and the raindrops observed by the aloft radar are assumed to fall vertically and mass invariably to the ground. This premise is obviously incorrect because it ignores a variety of microphysical processes when hydrometeors descend from the radar observation height to the ground, such as horizontal drift, evaporation, aggregation, melting, break up, collision, and coalescence (Dai & Han, 2014; Lack & Fox, 2007; Testik & Rahman, 2016, 2017). Albeit the importance of investigating the interaction between these microphysical processes as well as the associated meteorological elements and radar rainfall measurements is well recognized (Austin, 1987; Cluckie et al., 2000; Li & Srivastava, 2001; Pallardy & Fox, 2018), only a few studies addressed the relevant quantitative and practical methods by embedding the predominant raindrop evolution processes in radar rainfall adjustment (Dai & Han, 2014; Song et al., 2017).

In this work, we focused on two evolution processes of raindrops: horizontal motion and evaporation. There has been an increasing interest in radar rainfall uncertainty due to raindrop drift owing to developments in spatial radar rainfall resolution in recent years (Pallardy & Fox, 2018). After the out-of-sync issues with pixels between the radar and rain gauge were reported by Collier (1999), Mittermaier et al. (2004) presented the first quantified method to calculate wind-induced error by simulating fall streaks of snow. It was found that the order for the displacements could be as large as 10–20 km. Lack and Fox (2007) used a wind field simulated by radar observation itself to estimate the trajectories of falling drops and consequently adjusted the radar rainfall product. It was concluded that the impact of wind drift could be severe, especially at high spatial resolutions. Later, Lauri et al. (2012) presented a method to compute the horizontal displacement of hydrometeors using an advection scheme. Dai and Han (2014) simulated the motion of raindrops in the air by solving particle motion equations. The wind-induced errors of radar and rain gauge measurements were addressed by Lauri et al. (2012) and Dai and Han (2014), respectively, and new radar-gauge rainfall comparisons were constructed.

In terms of raindrop evaporation, Rosenfeld and Mintz (1988) and Li and Srivastava (2001) noted that raindrops could be considerably evaporated, especially for light-to-moderate rain in semiarid regions. Borowska et al. (2011) concluded that the observed increase in differential reflectivity (Z_{DR}) toward surface observations must be attributed to evaporation based on analysis of 1 month polarimetric radar measurements. To quantify the evaporation-induced error in radar rainfall estimation, Kumjian and Ryzhkov (2010) investigated the effect of raindrop evaporation on polarimetric radar parameters, including horizontal reflectivity (Z_H), Z_{DR}, and specific differential phase (K_{DP}) using a one-dimensional numerical model. They found that the evaporation rate that occurs in the subcloud layer has a close relationship with the initial shape of raindrops aloft. The model was later improved by Xie et al. (2016), who analyzed the amount of evaporation using a vertically pointing radar. Most recently, Pallardy and Fox (2018) simulated individual raindrops in the air using dual-polarization radar measurements and further concluded that raindrop evaporation played a significant role in radar rainfall estimation, especially in dry atmospheric environments.

Due to the motion and evaporation of raindrops, uncertainty is inevitably generated in directly intercepting radar rainfall aloft as surface rainfall. It is imperative to understand and identify the microphysical processes of raindrops and their impact on radar rainfall estimation. However, only a few studies have simulated raindrop evolution in a spatially variable atmospheric environment, and more importantly, a united framework to model both microphysical processes is still lacking. Therefore, this study proposes a fully formulated scheme to numerically simulate both the motion and evaporation of raindrops in a three-dimensional atmospheric context. This contributes to the improvement of quantitative precipitation estimation from radar polarimetry and allows a better understanding of the precipitation processes.

This paper is organized as follows. Section 2 illustrates the study area and data sources used. The Weather Research and Forecasting (WRF) model and raindrop size distribution model are also introduced in the context of this work. Section 3 presents the framework of the proposed scheme and describes the methods proposed for simulation and evaluation of raindrop microphysical processes. The results and validation are presented in section 4. A detailed discussion of these results appears in section 5. Finally, section 6 summarizes the key findings, limitations, and future work.

Table 1
Key Technical Specifications of the Radar

Parameters	Values
Antenna diameter	3.7 m
Beamwidth at half power	1°
Polarization	Linear H/V
Scanning type	Plan Position Indicator (PPI)
Scanning rate	1.4 revolutions per minute
Wavelength	5.3 cm (C band)
Peak power	250 kW
Maximum range	255 km
Location	Hameldon Hill, Lancashire, United Kingdom
Latitude	53°45′15″N
Longitude	2°17′11″W
Altitude	407 m MSL (Mean Sea Level)

2. Materials and Models

2.1. Study Area and Data Sources

The Hameldon Hill radar located in Lancashire, England (latitude 53°45′ 17″N, longitude 2°17′19″W) and its surrounding area were chosen as the study domain in this work. The radar system is a multiparameter C-band (5.3 cm wavelength) radar with simultaneous transmission and reception of horizontally and vertically polarized waves. The nominal beam width of the radar is 1° with typical gate resolutions of 300 and 600 m. The radar completes a series of scans with different angles every 5 min. The key technical specifications of the Hameldon Hill radar are listed in Table 1.

All the radar observables provides good, quantitative data that are reprojected to a Cartesian grid (based on the British National Grid coordinate system) spacing of 1 and 2 km, up to a range of approximately 50 and 75 km, respectively. The 1 km resolution data describe rain rate observations and provide the most detailed information, down to the scale of individual convective clouds (Met-Office, 2014). Data sets were received from mid-2014 by the Nimrod system, which is a very short-range forecasting system used by the Met Office. At the radar location, an on-site computer carries out aerial elevation control and digital signal processing. The radar rainfall data used in this study were supplied by the U.K. Met Office. The detailed description of the processing procedures can be found in Golding (1998) and Harrison et al. (2015). The raw data were processed by this Nimrod system, which incorporates extensive processing to correct the various sources of radar errors including noise, clutter, anomalous propagation, intervening rain attenuation, occultation, range attenuation, bright band, and orographic enhancement (Song et al., 2017). The detailed calibration of the dual-polarized reflectivity of the U.K. radar has been given by Gourley et al. (2009), which uses the consistency between radar reflectivity (Z_H), Z_{DR}, and the path integral of K_{DP} to calibrate the reflectivity. The dual-polarized signatures are used to estimate the raindrop size distribution (DSD) parameters. To obtain a more reliable outcome, three years (2015–2017) of disdrometer data were used to constrain the radar reflectivity range. Those values of radar reflectivity that not within the range calculated by disdrometer will be considered as incorrect values and be replaced by the interpolation of other values.

The gauge data sets were sourced from the Land and Marine Surface Stations Data (1853–current) of the Met Office Integrated Data Archive System. The data set comprises daily and hourly weather measurements, including rainfall measurements. A rain gauge network comprising 11 stations located within 50 km distance of the Hameldon Hill radar measures continuous hourly rainfall (see Figure 1). The indexes of the rain gauges are displayed in the figure. The station number is ordered based on its distance from the Hameldon Hill radar. The hourly gauge data of each of the 11 gauges were visually examined for each day of the year 2015, indicating that the gauge data were quality controlled to a high degree. The data sets are available from the National Centre for Atmospheric Science British Atmospheric Data Centre (Met-Office, 2012).

The meteorology data were sourced from the European reanalysis, European Centre for Medium-Range Weather Forecasts (ECMWF) Reanalysis ERA-Interim data set produced by the ECMWF. ERA-Interim is a reanalysis of the global atmosphere covering the data-rich period since 1979 and continuing in real time. It is considered one of the most significant atmospheric data sources for the scientific community (Dee et al., 2011). The data assimilation system used to produce ERA-Interim is based on the 2006 release of the Integrated Forecasting System, which includes a four-dimensional variational analysis with a 12 hr analysis window. The spatial resolution of the data sets is approximately 80 km on 60 vertical levels from the surface up to 0.1 hPa (Berrisford et al., 2011). ERA-Interim data can be downloaded from the ECMWF Public Data sets web interface, and detailed information (e.g., on current data availability) is available on the ECMWF website (at http://www.ecmwf.int/research/era). To ensure consistency in the radar and gauge data, 3 years of reanalysis data with 6 hr fields on an improved resolution of $1° \times 1°$ grid covering the Hameldon Hill radar and the surrounding area (with a range of 80 km to the radar center) were used. Three months of data were stored in a single file formatted by GRIB. The ERA-Interim data for the storm events were collected and retrieved separately. We selected ERA-Interim data because they are some of the most significant data

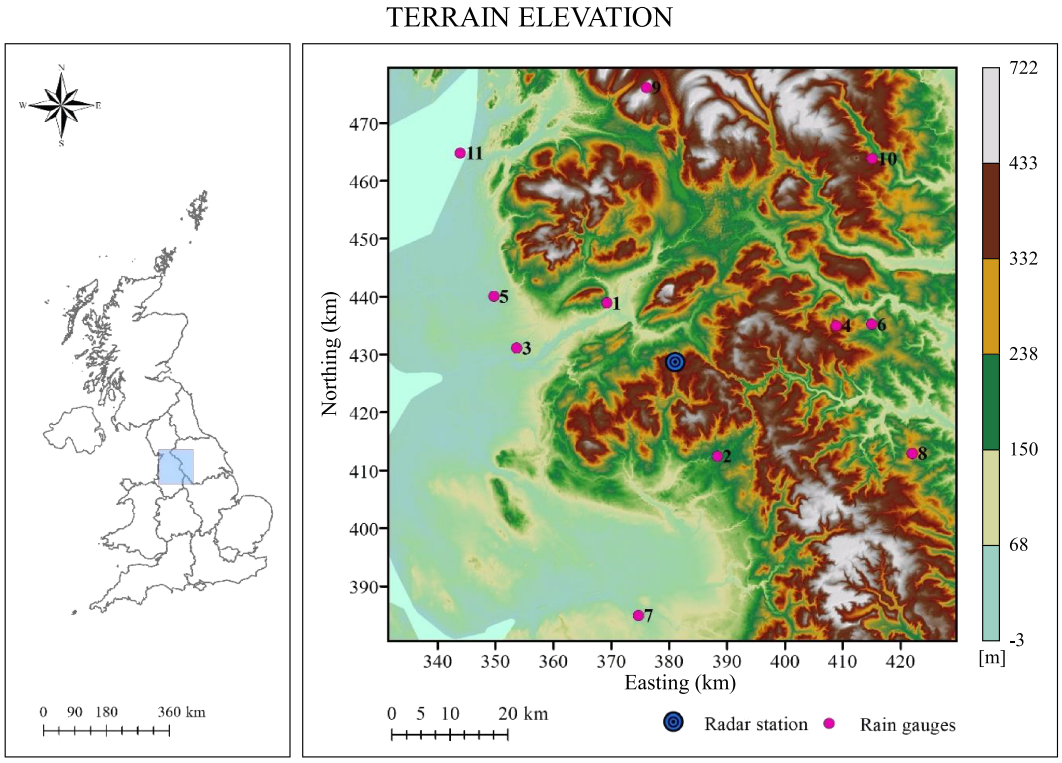

Figure 1. Map of the rain gauges, radar, and study area with terrain elevation in the background.

sources for the scientific community and encompass many essential climate variables in a physically consistent framework (Dee et al., 2011), which is significant to obtain the reliable three-dimensional atmospheric fields used in this study.

The coverage time range of each evaluation rainfall event must satisfy the maximum of the 11 rain gauges within the study area (100 × 100 km). In addition, we excluded the events where the radar, gauge, and dual-polarization data were not all available for the whole events. Finally, eight precipitation events were selected for the analysis to cover the period from 2015 to 2017. The relatively lighter rainfall events in the cold season were also included to ensure diversity. Event 1 in 2015 and Event 7 in 2016 were specifically used for graphics demonstration. Detailed descriptions of these events, including date, duration, and event-averaged rainfall, are presented in Table 2. To coordinate with the running of the WRF model, the start and end hours were set to 0, 6, 12, and 18.

2.2. The WRF Model

The WRF model (Powers et al., 2017) is a state-of-the-art mesoscale numerical weather prediction system designed for both atmospheric research and operational forecasts. It features two dynamical cores, a data assimilation system, and a software architecture supporting parallel computation and system extensibility. The WRF model is chosen because it has been developed and studied by a broad community of researchers and can be easily set up in each study area. In addition, the WRF model can perform simulations of local finer-scale atmospheric environments, which is referred to as "dynamical downscaling." In this work, the WRF model was configured to run with initial and boundary conditions taken from global reanalysis of ECMWF data sets. The three-dimensional atmospheric data generated from WRF were applied to raindrop microphysical simulation to estimate raindrop motion and evaporation. Among the WRF outputs, the following atmospheric fields are mainly used: horizontal wind (U for eastward and V for northward), vertical wind (W), perturbation geopotential (P_H), base-state geopotential (P_{HB}), terrain height (HGT), perturbation potential temperature (T), perturbation pressure (P), base state pressure (P_b), and water vapor mixing ratio (qv).

Table 2
Durations and Accumulated Rainfall for All Storm Events

Event ID	Storm start time	Storm end time	Duration (hr)	Accumulated rainfall (mm)
1	8 May 2015, 12:00:00	9 May 2015, 00:00:00	12	44.6
2	1 June 2015, 12:00:00	2 June 2015, 00:00:00	12	22.0
3	6 October 2015, 12:00:00	7 October 2015, 18:00:00	36	25.2
4	4 December 2015, 18:00:00	6 December 2015, 12:00:00	42	8.0
5	11 November 2016, 18:00:00	12 November 2016, 12:00:00	18	18.2
6	21 November 2016, 06:00:00	22 November 2016, 06:00:00	24	12.6
7	5 June 2017, 00:00:00	6 June 2017, 12:00:00	36	31.6
8	28 June 2017, 00:00:00	29 June 2017, 12:00:00	36	6.8

Note. The rainfall is accumulated by events and areal averaged for the study area.

The relative humidity (RH) used to calculate raindrop evaporation cannot be directly obtained from the WRF output. Instead, it is calculated using the water vapor mixing ratio as given in the following equation:

$$RH = 100 \times MAX(1, qv/qvs) \tag{1}$$

where qvs represents the saturation water vapor mixing ratio, and the function returns the argument with the largest value. This equation is concluded from the postprocessing system of the National Center for Atmospheric Research Command Language. As WRF uses the ERA levels to describe the vertical height, which are based on surface pressure and pressure at the top of the atmosphere, the layer height (LH) is computed as follows:

$$LH = \frac{(P_H + P_{HB})}{g} + HGT \tag{2}$$

where g represents the gravitational acceleration.

2.3. Raindrop Size Distribution Model

The DSD represents the distribution of the number of raindrops according to their diameters. It is typically expressed by mathematical functions such as the gamma or lognormal distributions (Feingold & Levin, 1986; Islam et al., 2012; Testik & Pei, 2017; Ulbrich, 1983). The DSD parameters in different locations and times are required as an initial condition of raindrop microphysical simulation. The advantage of dual-polarized radar has been the accurate retrieval of DSD parameters using a physical basis as opposed to statistical methods (Bringi et al., 2003). Benefiting from long-standing research, this study mainly uses previous outcomes pertaining to DSD retrieval from polarimetric radar measurements, especially Brandes et al. (2004) and Kim et al. (2010). The method treats the drop axis ratio as a variable and estimates the DSD parameters from radar reflectivity, differential reflectivity, and specific differential phase values.

To better describe the DSDs for small raindrops, a normalized form of gamma distribution, as described in Bringi et al. (2003), is used to represent rain DSD:

$$N(D) = N_w f(\mu)(D/D_0)^{\mu} \exp[-(3.67 + \mu)(D/D_0)] \tag{3}$$

where the parameter D is the diameter of the drop, D_0 represents the drop median volume diameter (mm), N_w denotes the normalized concentration parameter, and $f(\mu)$ is a function of the shape parameter (μ) given as

$$f(\mu) = \frac{6}{3.67^4} \frac{(\mu + 3.67)^{\mu+4}}{\Upsilon(\mu + 4)}. \tag{4}$$

The normalization form is free from any assumption of the shape of the raindrop spectra and could thus improve understanding of DSD (Testud et al., 2001). More importantly, polarimetric radar variables Z_{DR} and K_{DP} are dependent on D_0. In the present study, an empirical relation between D_0 and Z_{DR}, as

presented in Brandes et al. (2004), was established to derive D_0. Since μ is directly related to the median drop diameter D_0 by definition, μ can also be derived from Z_{DR}. D_0, μ, and water content W (g/m^3) are given by Brandes et al. (2004)

$$D_0 = 0.171Z_{DR}^3 - 0.725Z_{DR}^2 + 1.479Z_{DR} + 0.717 \tag{5}$$

$$\mu = 6.084{D_0}^2 - 29.85D_0 + 34.64, \tag{6}$$

$$W = 5.589\times10^{-4}Z_H\times10^{\left(0.223Z_{DR}^2 - 1.124Z_{DR}\right)} \tag{7}$$

Using D_0 and W, N_w can be estimated by the following equation (Kim et al., 2010):

$$N_w = \frac{3.67^4}{\pi\rho_w}\left(\frac{10^3 W}{D_0^4}\right) \tag{8}$$

where ρ_w is the water density (g/m^3). The DSD parameters estimated using the above equations are obtained for each radar pixel and time step (with spatial and temporal resolutions of 1 km and 5 min, respectively). The raindrop spectra are then used to drive the simulation of microphysical evolution.

It is worth remarking that other DSD parameter retrieving methods using polarimetric radar measurements exist, such as the "β method" proposed by Gorgucci et al. (2000) and Bringi et al. (2002). However, a comparison of different DSD retrieving methods is outside the scope of this study and has been researched by many past works (Anagnostou et al., 2008; Bringi et al., 2003; Gorgucci et al., 2002; Kim et al., 2010; Park et al., 2005).

3. Methodology

3.1. Model Structure

The discrepancy between radar and gauge rainfall is considered to be radar measurement error and is generally adjusted through statistical bias correction. The systematic bias is typically expressed in an additive or a multiplicative form using event-based, daily, monthly, or long-term radar-gauge pairs. If the radar and gauge measurements and the corrected radar product are represented by R, G, and ψ, respectively, the standard radar bias correction can be expressed as

$$\psi = R\times f[G, R] \tag{9}$$

where f is a function used to calculate the radar rainfall bias. For example, the function can be expressed as a ratio between the averaged radar and averaged gauge rainfall measurements over an accumulation period. The radar itself has measurement errors such as clutter, anomalous propagation, and bright band, and it is assumed that these have been corrected. The above equation assumes that the radar rainfall observed aloft is equal to the surface rainfall directly below the volume sampled by the radar beam. However, if the motion and evaporation of raindrops falling to the ground are considered, the above equation can be rewritten as

$$\psi = R\times f[G, \Gamma(R - E)] \tag{10}$$

where Γ is a transform function used to obtain the correct radar-gauge match. E is the missed rainfall due to the raindrop evaporation effect. All variables in the transform function Γ are expressed in the form of a three-dimensional matrix in projected space and time.

To compare the impact of different microphysical processes on the radar rainfall estimation, three models with different complexities of equation (10) are designed. The drift model (DM) omits E, which indicates that raindrop evaporation is ignored. Similarly, the evaporation model (EM) omits the transform function Γ, indicating that the raindrop motion is not included. The drift-evaporation integrated model (DEM) retains all items and thus represents both effects.

The key issue in DM is to derive the reconstruction matrix by simulating the raindrop drift process in the air and estimating the radar rainfall on the ground, which is fully discussed in section 3.2. The amount of

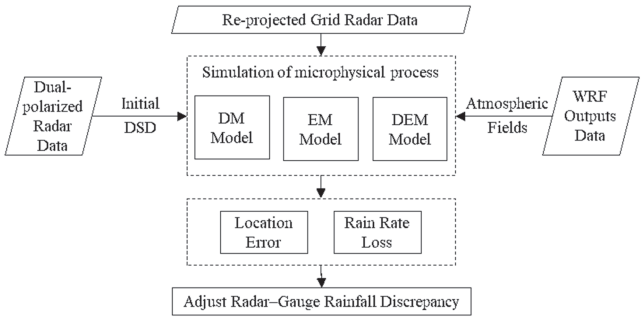

Figure 2. Adjustment procedure to resolve radar-gauge rainfall discrepancy using the WRF model and dual-polarization radar.

evaporated rain is derived by simulating the raindrop evaporation process, which is the major challenge in the EM and is discussed in section 3.3. Although these two processes are described separately, it is worth remarking that the DEM is implemented by integrating these two processes instead of cascading them. In each time step, the raindrop drift and evaporation are simulated independently, but the location change of the raindrop due to drift and mass change due to evaporation will affect the raindrop's microphysical processes in the next time step. A detailed discussion of the integration of these two processes is presented in section 3.4.

The adjustment procedure for radar-gauge rainfall discrepancy is based on the DM, EM, and DEM raindrop microphysical evolution models using the WRF model and dual-polarization radar displayed in Figure 2. The input data sets include the radar data before adjustment, the dual-polarization radar data used for retrieving the initial raindrop size distribution of each radar pixel, and the WRF output data provided the three-dimensional atmospheric fields. The location error and rain rate loss of each grid can be calculated through the DM, EM, or DEM raindrop microphysical simulation to adjust the radar-gauge rainfall discrepancy.

3.2. Simulation of the Raindrop Wind Drift Process

In this work, we assumed that each raindrop can be regarded as existing independently in the atmosphere, which means that it does not interfere with other particles. The possible uncertainty introduced under this assumption is discussed in section 5. To make the simulation of the raindrop microphysical process practical, the space between the ground surface and the height at which rainfall is observed by the radar is divided into multiple vertical layers (according to the 28 WRF terrain-following eta levels), and each layer is further divided into horizontal squared grids (1 km spatial resolution). With this discretization, the space is composed of a mass of conceptual three-dimensional subspaces whose location (with center coordinates of x, y, η) and resolution are configured to be equal to those of the WRF model. The atmospheric elements (such as wind and temperature) are assumed to be uniform within a subspace. To avoid boundary configuration, the boundary of the study area is extended by approximately 10 km to ensure that the raindrops would not move outside the space.

The tracing processes are carried out on the origins of 60 raindrops ranging from roughly 0.1 to 6.0 mm in diameter (at 0.1 mm interval). For each raindrop, the center point of the radar pixel is regarded as the initial horizontal coordinates. The height of the radar center beam corresponding to this point is configured as the initial height. The simple geometric method presented in Dai et al. (2013) is used to estimate the beam height.

Gravitational force and drag force by the wind are the main factors controlling the motion of raindrops in the air (Choi, 1997). The trajectories of the raindrops in each layer are traced separately by solving the particle motion equations as follows:

$$\begin{aligned} m\frac{\mathrm{d}^2x}{\mathrm{d}t^2} &= 6\pi\mu_a D\left(U-\frac{\mathrm{d}x}{\mathrm{d}t}\right)\frac{C_dR_e}{24} \\ m\frac{\mathrm{d}^2y}{\mathrm{d}t^2} &= 6\pi\mu_a D\left(V-\frac{\mathrm{d}y}{\mathrm{d}t}\right)\frac{C_dR_e}{24} \\ m\frac{\mathrm{d}^2\eta}{\mathrm{d}t^2} &= 6\pi\mu_a D\left(W-\frac{\mathrm{d}\eta}{\mathrm{d}t}\right)\frac{C_dR_e}{24}-mg\left(1-\frac{\rho_a}{\rho_w}\right) \end{aligned} \tag{11}$$

where m represents the mass of the raindrop, Re refers to the Reynolds number, ρa and ρw refer to the densities of air and water, respectively, and μ_a is the viscosity of air. U, V, and W are the WRF-derived wind fields in the x, y, and η directions, respectively. C_d denotes the drag coefficient of the raindrops. The equation used to estimate C_d was sourced from Chow et al. (1988).

The numerical simulation process is performed for each raindrop in each time step (e.g., 30 s). The displacements in the x and y directions for all time steps are accumulated separately. The procedure is iterated until

the raindrop moves outside the subspace and enters a new subspace. The final location of the raindrop is obtained until it reaches the ground surface.

The above simulation is carried out for all raindrops and radar pixels. The radar pixels, built based on the projection of the radar beam, are considered the original radar rainfall image. The adjusted radar pixels can be established based on the above simulation by recombining of the original radar rainfall image. In the adjusted radar rainfall image, the raindrops in each radar pixel stem from a series of radar pixels in the original image. Thus, the adjusted radar rainfall at a given pixel p can be derived using

$$\Gamma_p = \frac{\sum_{i=1}^{n} w_{p,i} R_i}{\sum_{i=1}^{n} w_{p,i}} \tag{12}$$

where i represents the index of the radar pixel where the raindrop drifts from pixel p and n is the total number of radar pixels. $w_{p,i}$ is the weight between radar pixel p and i, which is given as a function of the drop diameter D:

$$w_{p,i} = \sum_{j=1}^{m} N(D_j) D_j^3 \tag{13}$$

where D_j is a subset of raindrop spectra, indicating that these raindrops travel from radar pixel i to radar pixel p. The above equation is defined in such a form because the rain rate is proportional to the number and volume of raindrops (Bringi et al., 2003; Islam et al., 2012).

3.3. Simulation of the Raindrop Evaporation Process

A simple analytical solution for raindrop evaporation assumes that a prescribed steady environment is derived, which is presented by Rogers and Yau (1996) and Li and Srivastava (2001) and later applied by Kumjian and Ryzhkov (2010) and Pallardy and Fox (2018). If the vapor density at the drop surface exceeds the vapor density in the environment, the water vapor is diffused away from the rain drop. The rate of mass diffusion from a falling drop is expressed by Rogers and Yau (1996):

$$\frac{d_m}{d_t} = 2\pi D D_v f_v \Delta\rho_v \tag{14}$$

where d_m and d_t are the discrete form of raindrop mass and time, respectively. Dv is the diffusion coefficient of water vapor in air, and ρ_v is the difference in vapor density between the drop's surface and its environment. f_v is the diffusion and ventilation coefficient of water vapor in air, which can be expressed as a function of diffusivity, air viscosity μ_a, raindrop diameter, and terminal fall velocity of the raindrop V:

$$f_v = 0.78 + 0.308(v/D_v)^{1/3}(VD/v)^{1/2} \tag{15}$$

The change in diameter dD is then estimated using

$$VD\frac{\mathrm{d}D}{\mathrm{d}z} = \frac{4}{\rho_w} D_v f_v \Delta\rho_v \tag{16}$$

where the vertical coordinate z is measured downward, from the start of the time step to the end. The estimation of ρ_v can be found in Li and Srivastava (2001). The change in the diameter of the raindrop is calculated for each time step until the raindrop totally evaporates or reaches the ground. A new raindrop size distribution on the ground can be obtained by modeling the evaporation processes for all raindrops within a radar pixel. The rain rate loss E due to evaporation is estimated by comparing the raindrop mass before and after the evaporation process.

3.4. Integrating the Simulations of Raindrop Drift and Evaporation Processes

In the DEM scheme, the initial raindrop size distribution and location are obtained using the same approach as the individual process models of drift and evaporation. In this scheme, the motion of the raindrop and its change in diameter (due to evaporation) are simulated alternately. More specifically, after a new position

and velocity of the raindrops are simulated at the end of each time step, the change in drop diameter is estimated based on the raindrop evaporation model, and the new drop diameter is used in the next time step.

As both the location and mass of the raindrop may change when it reaches the ground, the adjusted radar rainfall is derived using the following equation:

$$\Gamma_p = \frac{\sum_{i=1}^{n} w_{p,i}(R_i - E_i)}{\sum_{i=1}^{n} w_{p,i}} \tag{17}$$

The calculation of weights is also based on equation (13). With the simulation of trajectories and evolution of raindrops in all radar pixels, the adjusted radar rainfall is regarded as the "true" ground surface rainfall observed by radar. Although the radar-gauge pairs are still built based on the projected location of the radar beam, a more complicated and rational spatial relationship between them is considered.

3.5. Evaluation Method

As mentioned above, part of the discrepancy between radar and gauge rainfall measurements is the error due to the raindrop microphysical evolution. Therefore, an adjustment in radar rainfall error induced by raindrop evolution will improve consistency between radar and gauge rainfall measurements. As a result of this, the evaluation method is designed by calculating the indicators related to the radar-gauge rainfall differences.

Four indicators were used in this study, namely, the Spearman rank correlation coefficient (*SRC*), fractional absolute difference (*FAD*), hit ratio (*HR*), and false alarm ratio (*FAR*). The *SRC* is equivalent to the Pearson's linear correlation coefficient applied to the rankings of the variables. If all the ranks in each variable are distinct, the *SRC* is defined as follows:

$$SRC = 1 - \frac{6\sum d^2}{k(k^2-1)} \tag{18}$$

where d is the difference between the ranks of the two variables and k is the length of each variable. The range of *SRC* is [−1, 1], and a higher value corresponds to a higher positive correlation. The *SRC* is used to reflect the degree of match between the radar and gauge rainfall measurements (Cecinati et al., 2017; Germann et al., 2009; Habib et al., 2008).

As the correlation cannot reveal the radar-gauge absolute bias, the fractional absolute difference is introduced, which is written as

$$FAD = \frac{1}{k}\sum_{i=1}^{k} \frac{|R_i - G_i|}{G_i} \tag{19}$$

where R and G are the radar-estimated and gauge rainfall, respectively, and k is the total number of rainfall events.

It was found that the occurrence ratio of rainy pixels may change after the adjustment of radar rainfall. Both raindrop drift and evaporation adjustment may cause the rainfall to decrease to 0 in the original rainy radar pixels. As the ability to determine rain or lack of it is an important aspect of radar rainfall measurement, *HR* and *FAR* are also calculated. They are defined as follows:

$$HR = \frac{N_a}{N_a + N_c} \tag{20}$$

$$FAR = \frac{N_b}{N_a + N_b} \tag{21}$$

where N_a is the number of correct rain forecasts (hits), N_b is the number of false alarms, N_c is the number of misses. N_a, N_b, and N_c are the entries of a contingency table of the radar rainfall measurement against gauge observations, which are presented in Table 3. The rainfall threshold value to define rain/no rain used in this study is 0.1 mm/hr. According to the definition of hit and false alarm rates, a perfect rainfall product should have $HR = 1$ and $FAR = 0$.

Table 3
Rain/No Rain Contingency Table of the Radar Rainfall Measurement Against Gauge Observations

	Rain	No rain
Rain	N_a (hits)	N_b (false alarms)
No rain	N_c (misses)	N_d (correct negatives)

3.6. Calculation of Three-Dimensional Atmospheric Fields Using the WRF Model

The three-dimensional atmospheric fields were estimated using the WRF model with Advanced Research WRF dynamic core, version 3.8. The WRF model was used to downscale the ERA-interim reanalysis data for eight storm events, where each event has a 24 hr warm-up.

The simulations were performed using the WRF model with the following physical options: the Thompson aerosol-aware scheme microphysical parameterization (Thompson & Eidhammer, 2014), the RRTM longwave radiation scheme (Mlawer et al., 1997), the Dudhia shortwave radiation scheme (Dudhia, 1989), the Kain-Fritsch cumulus scheme (Kain, 2004), the Mellor-Yamada-Janjic planetary boundary layer scheme (Janjić, 1994), and the Noah-MP land surface model (Niu et al., 2011). Additional options from the version of WRF intended for climate applications were also incorporated.

The spatial setup of the WRF model is composed of two domains centered at the Hameldon Hill radar with a downscaling ratio of 1:5. A detailed description of the domain configuration is presented in Table 4. The 25 km domain covers most of the United Kingdom, and the 5 km one-way nested domain covers the extent of radar measurement. The Lambert conformal conic projection was used as the model horizontal coordinates. In the vertical direction, we used 28 terrain-following eta levels, with the top level set at 50 hPa. The model was designed with 0.5 hr downscaling temporal resolutions with interpolation from the 6 hr ECMWF data. The atmospheric fields associated with DSD evolution (including wind, temperature, and relative humidity) were obtained in the outputs of Domain 2 with 5 km spatial and 0.5 hr temporal resolutions. During the simulation process of raindrop wind drift and evaporation, these atmospheric fields will be projected to 1 km grids (the same as in the case of the radar).

4. Results

4.1. Calculation of DSD by Dual-Polarization Radar

The DSD that governs the initial raindrops spectra was estimated using dual-polarization radar measurements. The change in DSD parameters with time for two events is shown in Figure 3. All the relevant parameters, namely, D_o, dBN_w ($dBN_w = \log_{10}(N_w)$), and μ, are plotted. The value was averaged over the study area for all rainy radar pixels with a temporal resolution of 5 min. The DSDs in most radar pixels can be retrieved using the polarimetric radar variables Z_H and Z_{DR} (see section 2.3). However, the retrieved method cannot derive all DSDs for all radar pixels. The pixels with missing Z_H or Z_{DR} are estimated using the neighboring pixels. For the first event, small drops (low D_o) of a large number (high dBN_w) were observed in most time steps, especially during the middle event. A different trend in the parameters was observed in the second event, during which relatively larger volume-averaged drops were found (see Figure 3b). Temporal variation in the parameters in the second event were more intense than those in the first event, particularly for the parameter μ.

A fixed DSD is commonly used in current radar rainfall estimations and raindrop evolution simulations (Dai & Han, 2014). Considering the large differences of all three parameters between two events, a fixed DSD parameter will introduce a large uncertainty in the simulation of microphysical processes. Therefore, the variational DSD over space and time used in this study is considered more reliable.

4.2. Simulation of Raindrop Microphysical Processes

The raindrop drift and evaporation processes were simulated by numerical iteration within the three-dimensional atmospheric environment using the height of the raindrop observed by the radar to the ground level. The simulation was carried out for a range of raindrop sizes at each pixel and time step. The spatial and temporal resolutions of the simulation were configured to 1 km (the same as the radar) and 0.5 hr (the same as that for the WRF model), respectively. Within the space and time unit, the atmospheric conditions associated with the DSD evolution are regarded as consistent. In each simulation, the time step of the numerical iteration was set to 30 s.

Table 4
Configurations of the WRF Model for Three Nested Domains

Domain	Domain size (km)	Grid Spacing (km)	Grid size	Downscaling ratio
d01	11 * 360	25	21 * 21	—
d02	175 * 175	5	35 * 35	1:5

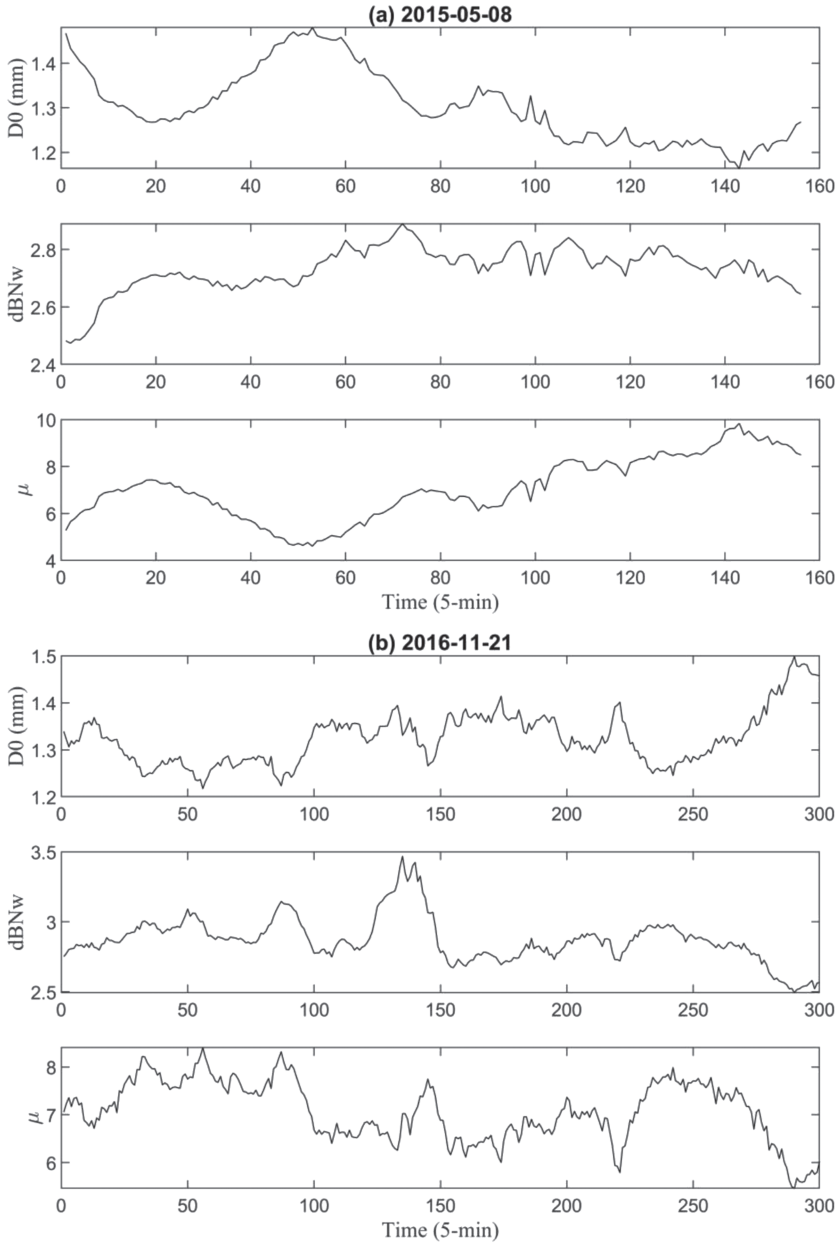

Figure 3. Time series plot of median diameter D_o, intercept parameter N_w, and shape parameter μ for the (a) 8 May 2015 event and (b) 21 November 2016 event, respectively.

Comparisons of the final horizontal drift and ground wind are shown in Figures 4 and 5 for Events 1 and 3. These two events were selected for demonstration owing to their representative wind conditions. The figures in the first column refer to the ground wind at different times (unit: m/s), and the remaining figures represent the raindrops drift for raindrop diameters of 0.2, 1, and 5 mm. The start and end points of the drift arrows are the real projected locations of the raindrops on the ground. The arrows are not shown in the figure if the raindrops drift outside the study domain. Some arrows in the drift map of the 5 mm raindrop in Figure 4 are missing. This is because the drift distance is less than 0.5 km, which means that the raindrop will stay within the radar pixel it originates in. There are obvious different patterns of wind fields within and between these two events. In Event 1, the wind fields generally blow to the northwest corner of the study domain. More specifically, part of the wind direction is west forward, and another part is northwest forward. The last time step of Event 1 (8 May 2015, 20:00) shows some wind fields pointing almost north. The change in wind in Event 3 is not so remarkable; the wind generally blows from northeast to southwest.

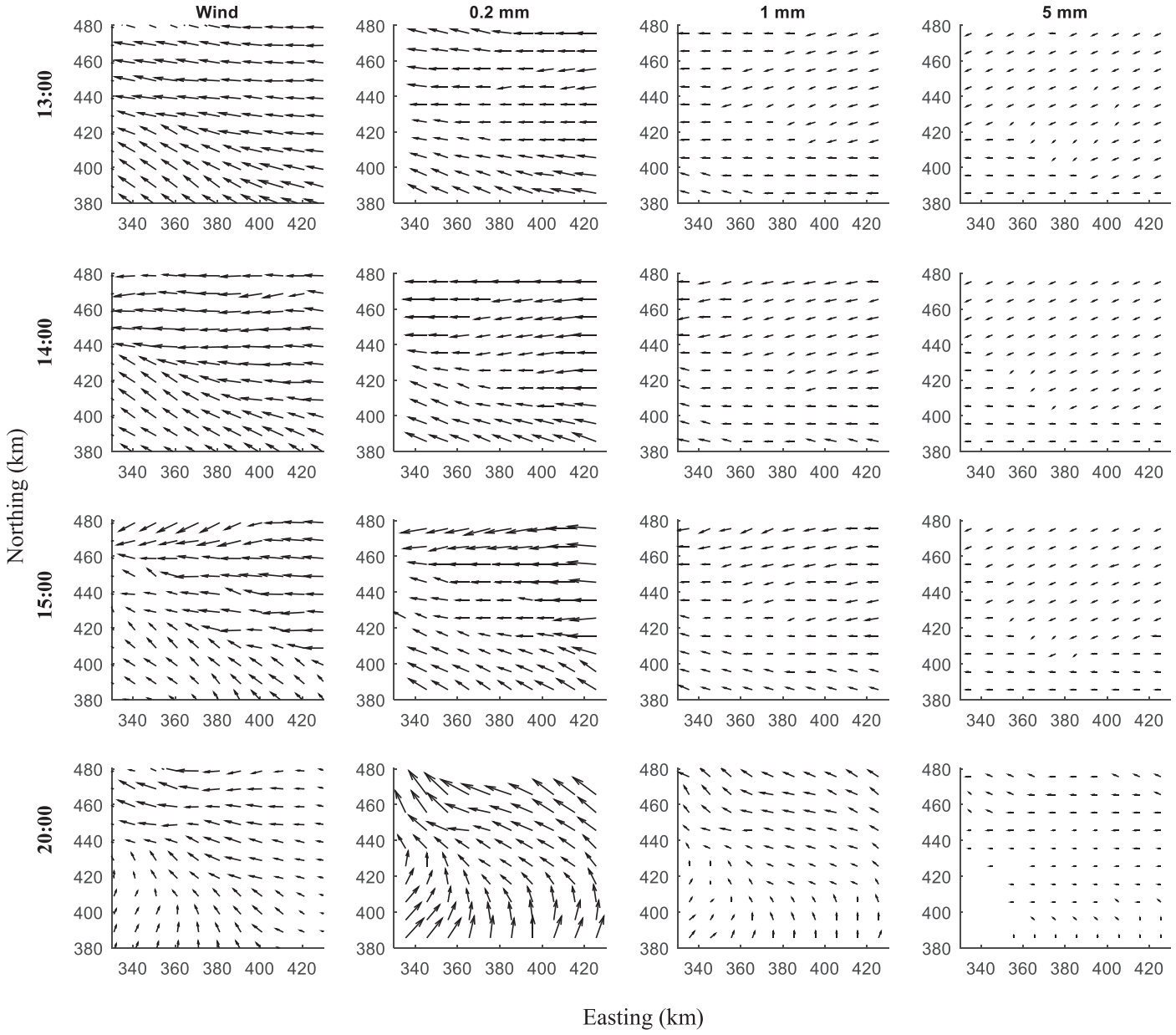

Figure 4. Maps of ground wind and raindrop drifts for sizes 0.2, 1, and 5 mm for different time steps for the 8 May 2015 event.

The general patterns of raindrop drift are quite close to the corresponding wind fields. However, there are many deviations, or even conflicts, between them at some locations. For example, a comparison of the drift map of the 0.2 mm raindrop with the wind field in the first time step of Event 1 (8 May 2015, 13:00) shows that the drift directions in the southwest part of the domain are inclined to point west instead of northwest. This trend is more obvious for the drift maps of the 1 and 5 mm raindrops. Moreover, noticeable differences between the drift and wind maps are found in the last time step, especially in the eastern part of the study area. These deviations are reasonable because the wind field only records the ground surface wind, whereas the raindrop drift is the consequence of the integrative impact of wind from the radar beam to the ground, which has been proved by checking the vertical profiles of the wind direction. This result proves that there is considerable uncertainty associated with raindrop evolution using solely ground wind observations.

In terms of the drift distance, the relationships between area-averaged drift distance and wind speed for different drop sizes are shown in Figure 6. The drift distances are calculated using the real cases of all eight

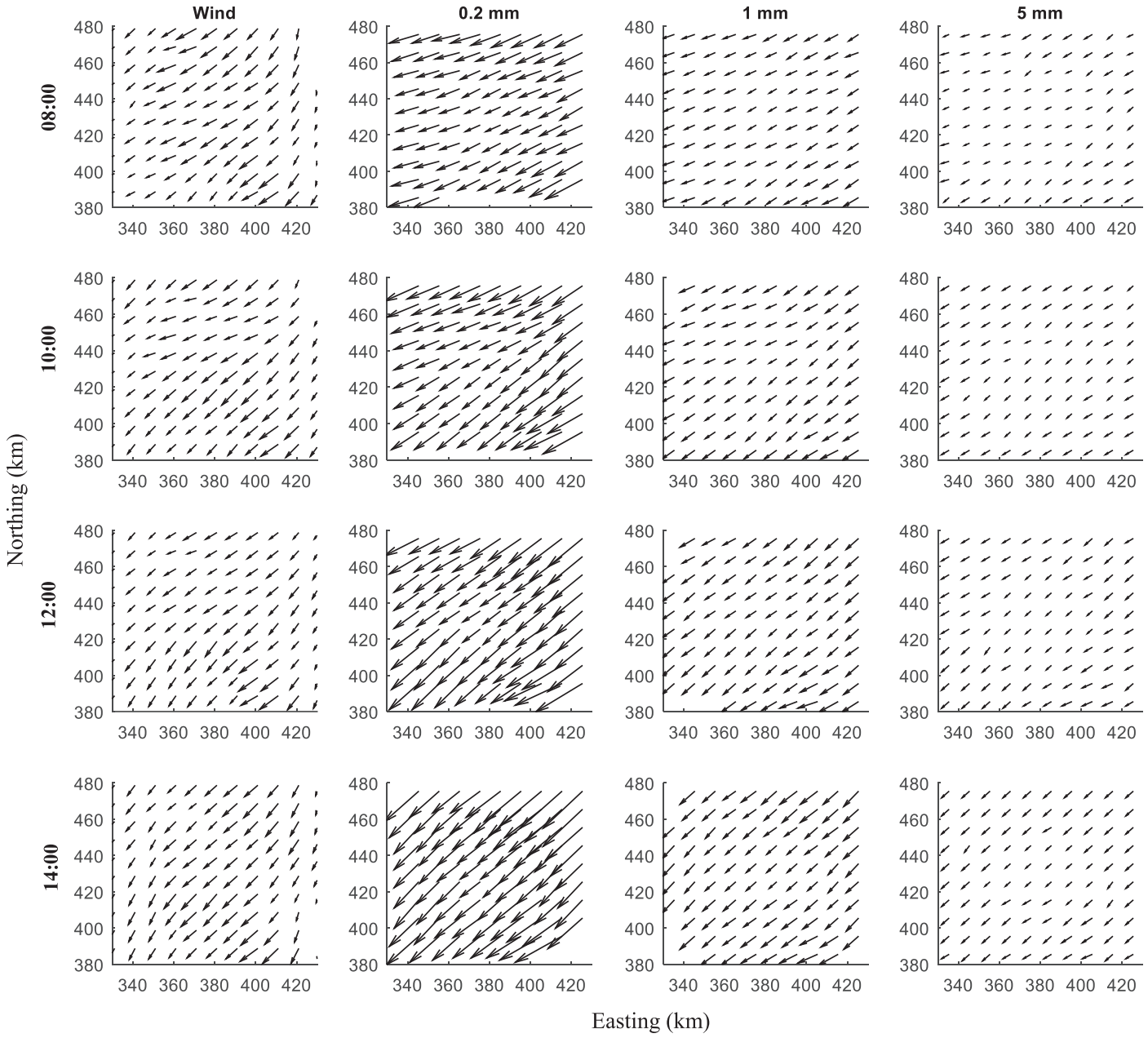

Figure 5. The same as Figure 4 but for the 21 November 2016 event.

events. One can observe that the drift distance decreases with the increase in the raindrop size at the same wind speed. This is because the falling speed of the raindrop is positively correlated with its diameter, and consequently, the time of raindrop motion in the air decreases with the increase in the raindrop diameter covering the same vertical distance. In addition, the drift distance obviously increases with the wind speed, but at different ratios for different raindrop sizes. The ranges of drift distance for raindrop sizes of 0.2, 1, and 5 mm are approximately 1.5–14, 1–7, and 0.1–4 km, respectively, indicating that the variation in the drift distance decreases significantly with the increase in the raindrops.

4.3. Radar Rainfall Adjustment Considering the Raindrop Microphysical Process

The radar rainfall images on the ground surface are derived by considering the raindrop drift, evaporation, and both aspects. A comparison of the corrected images (based on DM, EM, and DEM) and the original one

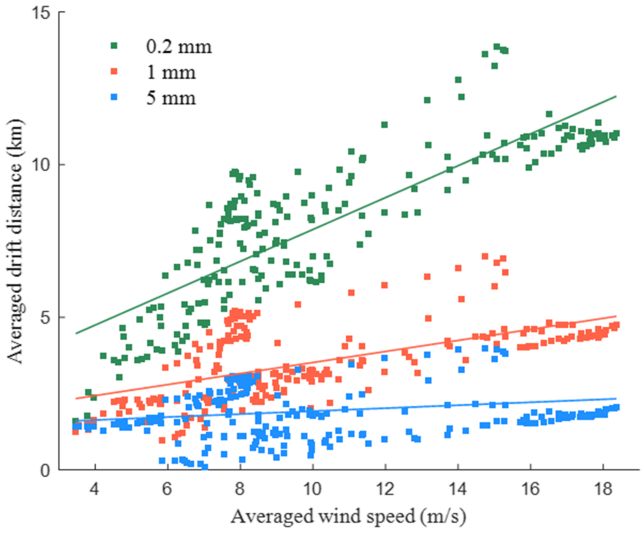

Figure 6. Relationship between averaged wind speed and drift distance for different raindrop sizes.

for Events 1 and 3 are shown in Figures 7 and 8, respectively. In these figures, the spatial and temporal resolutions are 1 km and 5 min for all radar rainfall images, respectively. The time for each figure corresponds exactly to that of the wind field in Figures 4 and 5. The images of each time step are displayed with individual color maps to better illustrate the differences between radar images using different adjusted models.

A comparison of the drifted radar images (DM) with the original images indicates that the drift directions mainly follow the wind direction in Figures 4 and 5, although the drift direction and distance cannot be observed apparently at first glance from these large-scaled images. For example, the drifted images move southwest compared to the original radar images in Figure 7. Many hints on the images (marked as red lines) confirm this reasoning. In addition, many pixels do not show rain in the original image but do so in the drift image. This is because the different sizes of raindrops have different drift distances, and part of the raindrops in the rainy pixels may drift to the no-rainy pixels in the original radar image. This phenomenon can only be observed at the boundary of the cluster of rainy pixels.

For the evaporation images derived using the EM scheme, all the overall values are less than the original radar rainfall. It is worth remarking that the DM adjustment will not affect the rainfall balance of the entire study area, whereas the EM adjustment causes various degrees of mass loss of rainfall. One can observe a significant mass loss of rainfall in Event 1 (see Figure 7). This loss is relatively small in Event 3 (see Figure 8).

The combined effect of raindrop drift and evaporation on radar rainfall are studied using DEM adjustment and shown in the last column of the group images. The images show that the extent and quantity of the rainy domain are similar to those in the drift images and evaporation images, respectively. However, the combined effect does not denote a simple refactoring of the drift and evaporation radar image. In DEM adjustment, the size of the raindrop will change in each iteration before drifting. The raindrop may completely disappear before it reaches the ground. Such cases will certainly not have a drift process.

4.4. Comparison of Radar-Gauge Rainfall and Evaluation of the Proposed Method

To evaluate the proposed method under different configurations (DM, EM, and DEM), a series of comparisons were carried out using ground surface rainfall from a rain gauge network as reference values. First, the hourly accumulation radar with 1 km spatial resolution and gauge rainfall estimations are compared for different events at two gauge locations as shown in Figures 9 and 10. The black dash-dot line and red dotted line refer to the measured gauge and radar rainfall, whereas the other lines denote corrected radar rainfall. Compared to the gauge rainfall of DM and DEM radar rainfall values, the absolute errors are smaller than the original values and EM results in most cases. For the time steps with high rainfall rate (e.g., 4 mm/hr), the original value exhibits the worst or second-worst performance compared to the DM, EM, and DEM outputs, such as Event c at Gauge 2 and Event a at Gauge 9 (see Figures 9c and 10a).

The correlation coefficients, *FAD*, *HR*, and *FAR*, are then calculated to quantify the performance of four types of radar rainfall adjustments. In Figure 11, the correlation coefficients between the original radar and gauge rainfall at different gauge locations are displayed using hollow red dashed circle, whereas those between the corrected radar and gauge are represented using other colors. With a few exceptions, the original radar rainfall has the least correlation with the gauge rainfall. The highest correlation coefficient varies for different times and locations. The DEM adjustment tends to perform best in Events c and d at 50% gauges.

In terms of the FAD, as shown in Figure 12, the original radar rainfall has the worst performance (36.4% of the proportion), followed by the EM (27.2%), and the radar rainfall values of both DM (18.2%) and DEM (18.2%) are relatively better. As there is no considerable difference in the *HR* and *FAR* values within these events, we did not present them here.

The detailed values of these indicators are listed in Tables 5–7. The values are averaged over all gauges for each event. The correlation coefficients of all corrected radar rainfall values are generally better than the

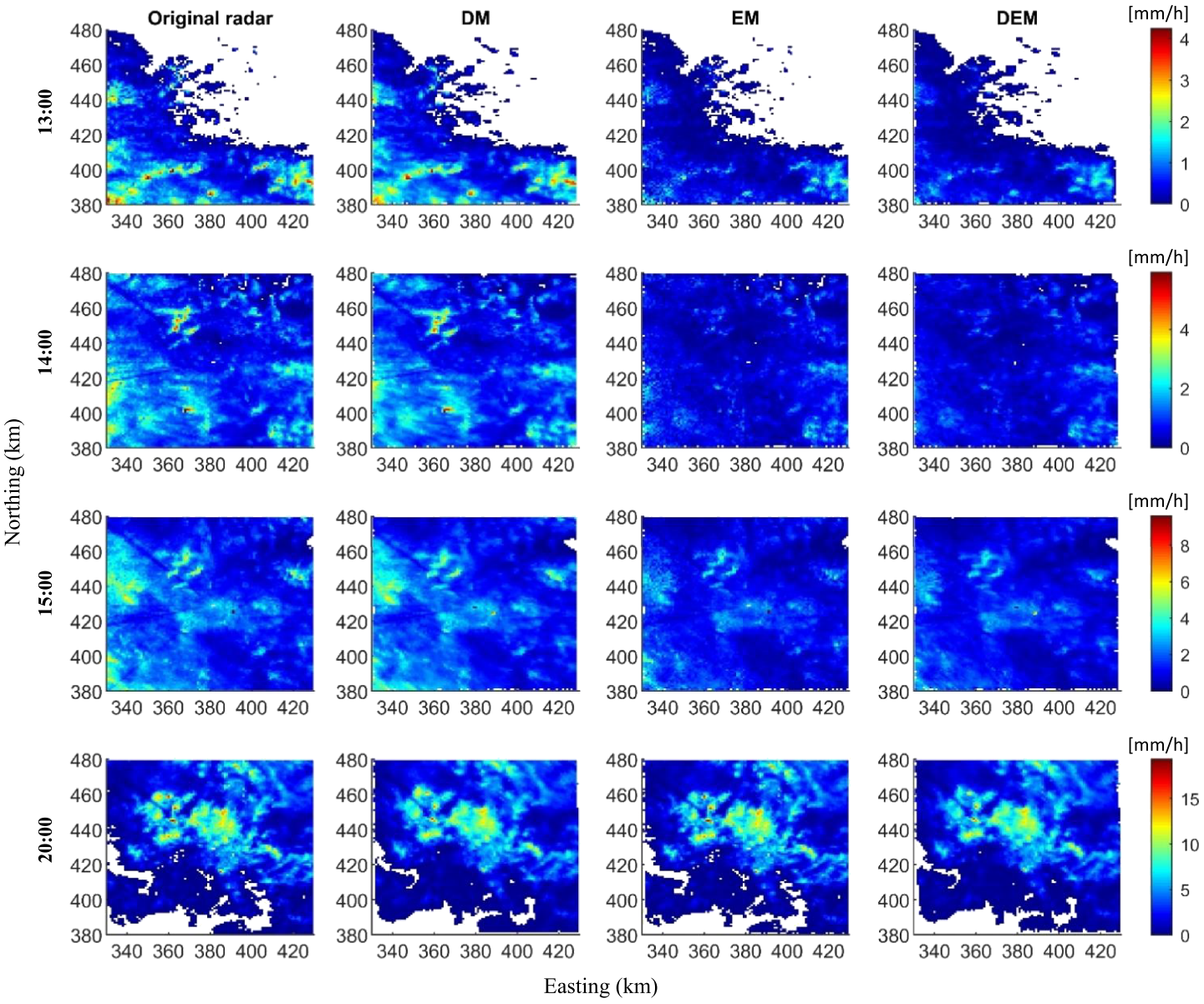

Figure 7. Comparisons of original and adjusted radar images (using the DM, EM, and DEM models, respectively) for different time steps for the 8 May 2015 event.

original values. For example, the DM adjustment increases the correlation from the original 0.75 to 0.81 in Event 6, which denotes an improvement of 8.0% over the original value. In Event 6, the EM scheme improves the correlation from 0.75 to 0.79, denoting an improvement of 5.3%. The maximum enhancement for the DEM is observed in Event 8, which also shows an improvement of 7.2%. The increases in the correlation coefficients are 3.2%, 2.9%, and 3.8%, on average, for all time steps and locations of DM, EM, and DEM, respectively.

Moreover, all radar rainfall events using DM and DEM adjustments and 75% radar rainfall events using EM adjustment show lower FAD values than their original counterparts. For example, the DM, EM, and DEM schemes can reduce the discrepancy by 42.6%, 16.0%, and 53.2%, respectively, compared to the original FAD values in Event 4. The DEM scheme reduces radar-gauge discrepancy by 21.7% averagely for all rainfall events. Overall, there is no significant difference in the *HR* and *FAR* between the four types of radar rainfall. Three schemes only exhibit a slightly worse performance for Event 3 in terms of *HR* and for Event 5 in terms of *FAR* (see Table 7). It is concluded that the radar adjustment approach indeed improves the match with the radar-gauge match.

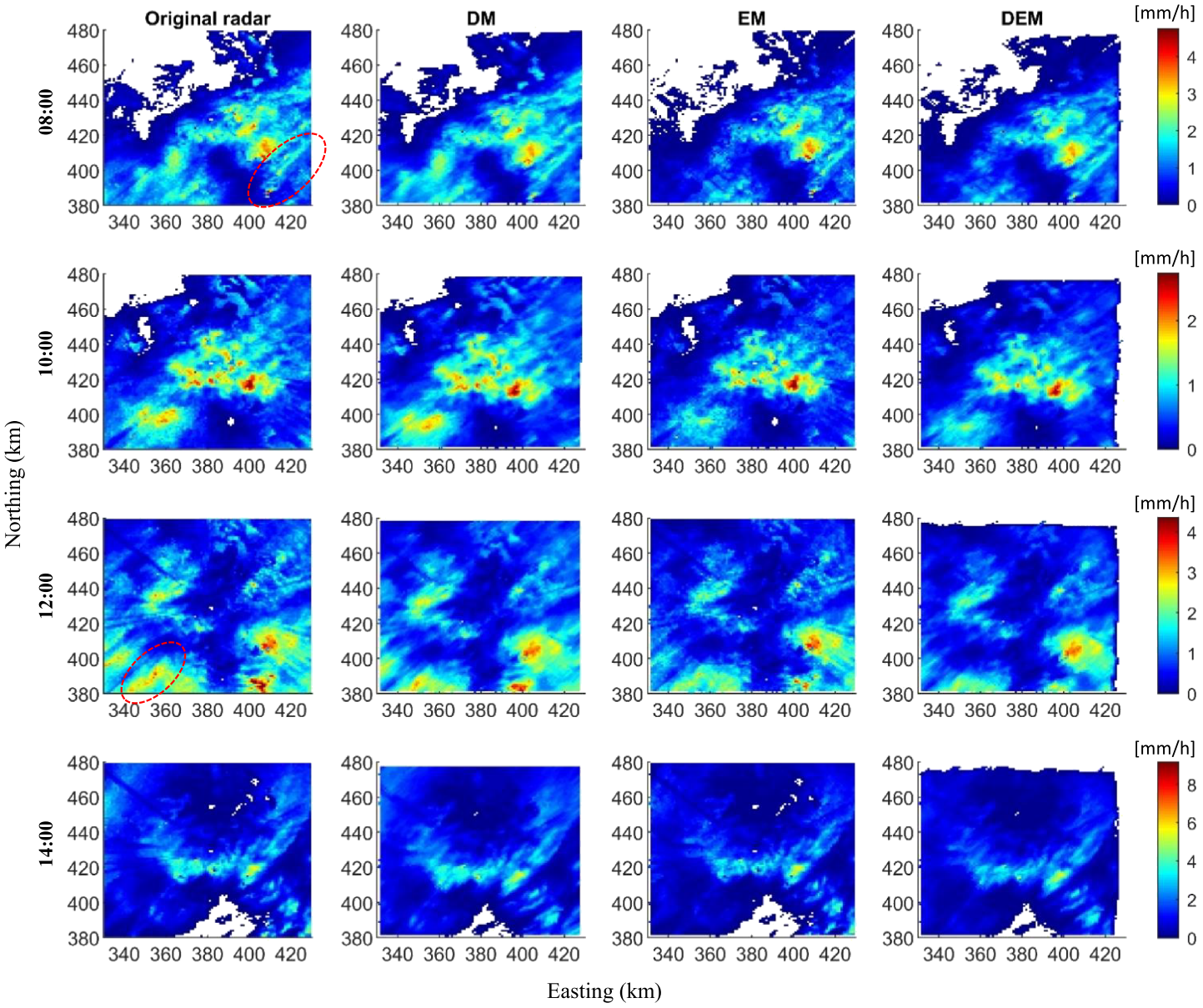

Figure 8. The same as Figure 7 but for the 21 November 2016 event.

5. Discussion

The impact of raindrop motion and evaporation on radar rainfall measurement has been recognized for years (Collier, 1999; Li & Srivastava, 2001). Despite its importance, this issue is not considered or addressed in the most up-to-date radar rainfall quality control experiments (Lauri et al., 2012; Xie et al., 2016). This is because the induced errors are considered insignificant compared to ground clutter, beam blockage, and vertical variability of reflectivity, and the complicated process experienced by a real raindrop is difficult to model. The results of this work indicate that the radar rainfall estimated error induced by two microphysical processes, namely raindrop drift and evaporation, cannot be ignored. For example, the drift distance can reach 14 km for a raindrop size of 0.2 mm, and 5 km for one with a size of 1 mm. An obvious fall in rainfall intensity due to evaporation adjustment was also noted in Figures 7 and 8. More importantly, an improvement in radar rainfall performance is observed in most events. Therefore, it can be concluded that the radar rainfall error induced by the microphysical processes of raindrop drift and evaporation cannot be ignored.

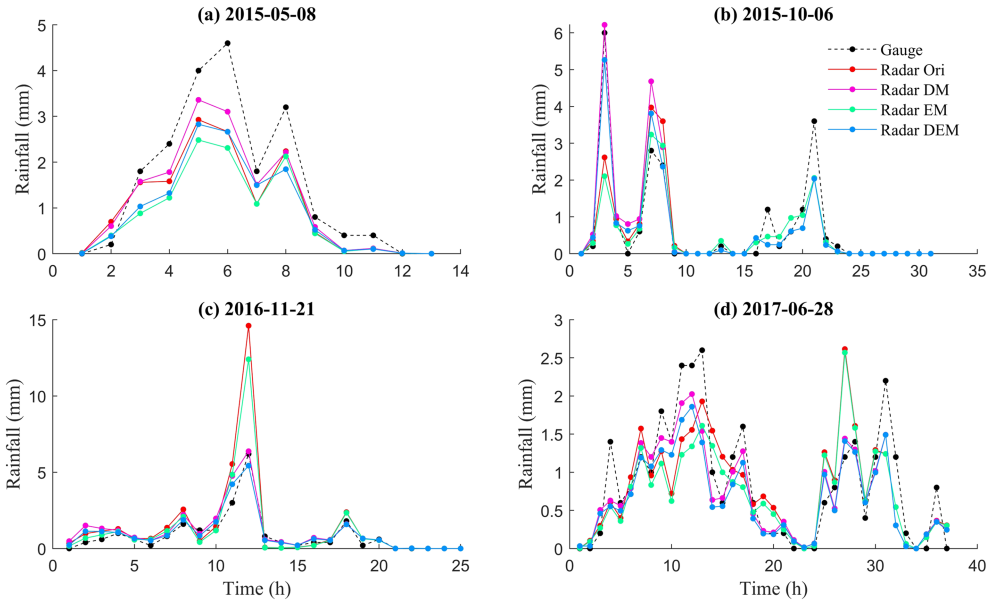

Figure 9. Time series plot of rain gauge, and original and adjusted radar rainfall values for different events at Gauge 2. On dates (a) 8 May 2015, (b) 6 October 2015, (c) 21 November 2016, and (d) 28 June 2017.

The novelty of this study can be summarized by the following three points: 1) in comparison to the work by Dai and Han (2014), which assumed that the raindrops within a pixel can only drift to a single location, this work simulates raindrop movement using a varying raindrop size distribution obtained from a dual-polarization radar; 2) few studies have quantified the possible error induced by raindrop evaporation on radar-gauge comparison. We believe that the proposed scheme for the adjustment of evaporated induced error offers valuable insights to the scientific community; 3) this is the first study that numerically simulated the motion and evaporation of raindrops in a three-dimensional atmospheric context.

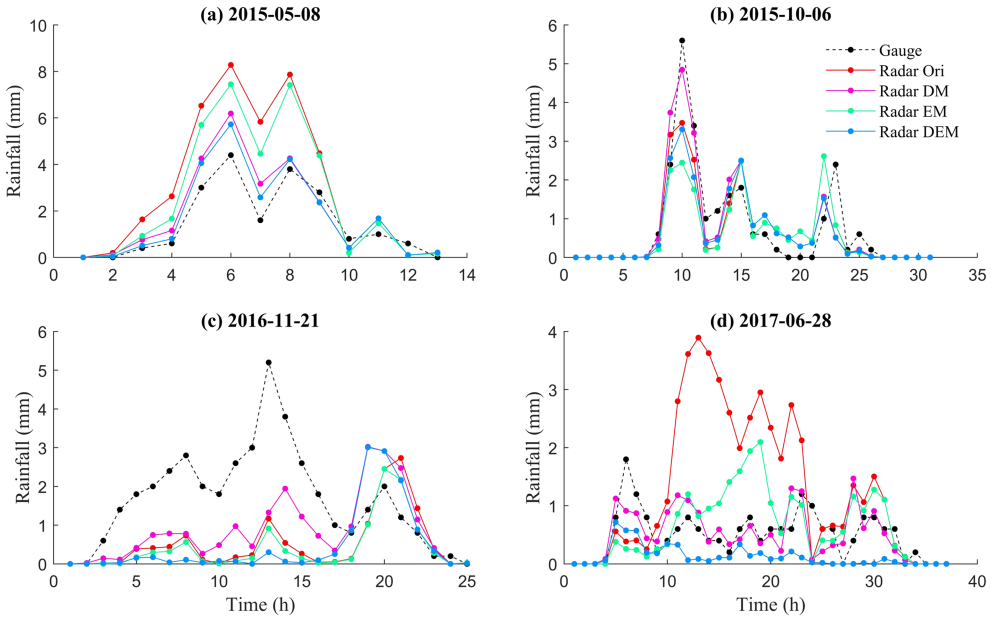

Figure 10. The same as Figure 9 but for Gauge 9.

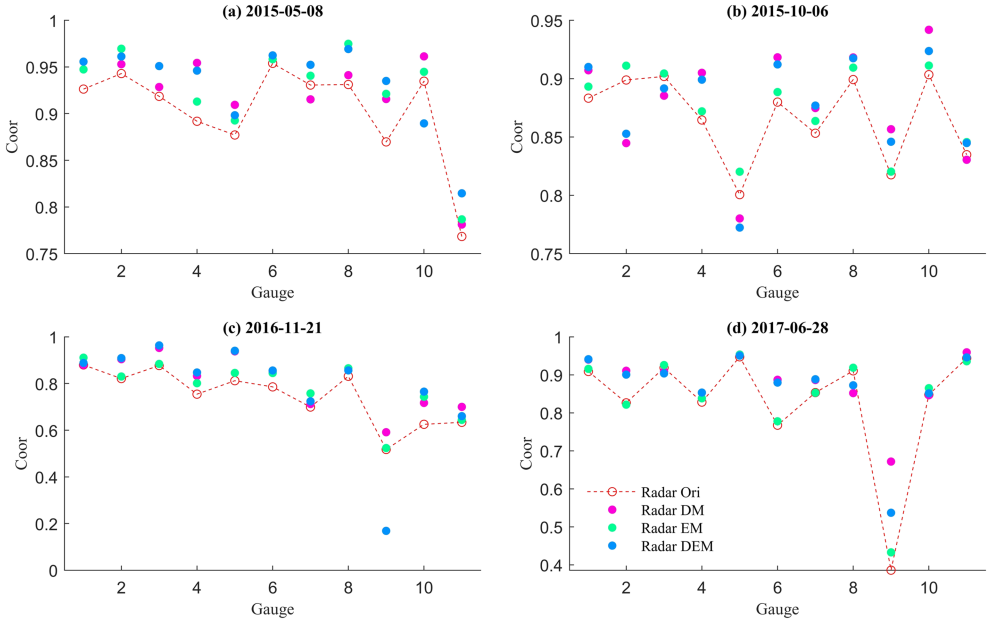

Figure 11. Comparisons of correlation coefficients between rain gauge rainfall and various radar rainfall estimates (original, DM, EM, and DEM) for different locations and events. On dates (a) 8 May 2015, (b) 6 October 2015, (c) 21 November 2016, and (d) 28 June 2017.

However, some limitations admittedly exist, indicating the uncertainty associated with the proposed scheme. From our point of view, the uncertainty originates from, but is not confined to, the initial conditions of the raindrops, such as location, DSD, and sampling, and a series of simplifications in simulating the evolution of the raindrops. The first issue may be considered via a comparison of the impact of the top, center, and bottom beams of the radar on the wind drift simulation, as demonstrated in Dai and Han (2014). It was

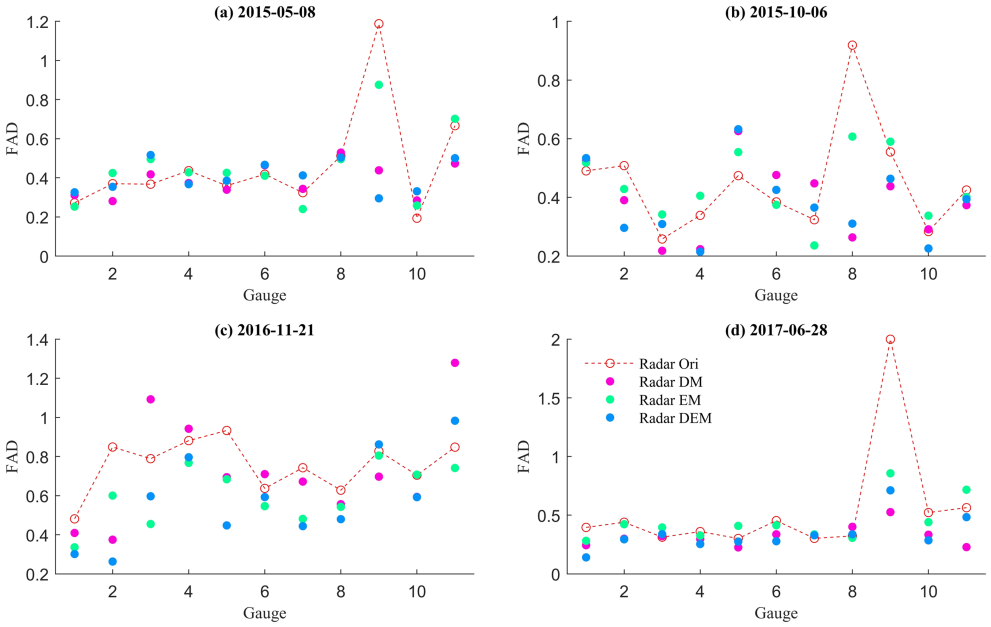

Figure 12. Comparisons of FAD values of various radar rainfall estimates (original, DM, EM, and DEM) using rain gauge rainfall as the reference for different locations and events. On dates (a) 8 May 2015, (b) 6 October 2015, (c) 21 November 2016, and (d) 28 June 2017.

Table 5
Correlation Coefficients Between Radar and Gauge Rainfall Measurements for All Events

Event	Original	DM	EM	DEM
1	0.90	0.93	0.93	0.94
2	0.86	0.89	0.91	0.90
3	0.87	0.88	0.88	0.89
4	0.83	0.85	0.86	0.88
5	0.88	0.88	0.90	0.90
6	0.75	0.81	0.79	0.80
7	0.79	0.80	0.82	0.82
8	0.83	0.88	0.84	0.89

found that the differences in radar-gauge rainfall correlation between the three beam heights for most time steps are small. To obtain a more reliable DSD, the modern dual-polarization radar is used. The so-retrieved DSD is also subject to a series of uncertainties (Kim et al., 2010), but it can better reflect the real DSD spectra than predefined and fixed DSD. The DSD spectra should cover a range of 0.1–6 mm with an interval of 0.1 mm to elaborately model the variation among different raindrops. All these efforts are intended to arrive at a better initial condition for the model. However, more work is needed.

Other errors may affect the adjustment and validation process of this work. One of the major concerns is the uncertainty originated from the meteorological data sets, that is, the ERA-Interim data used to drive the WRF model. If the value of meteorological data significantly deviates from the true weather condition, the adjustment results will be unreliable, and the error of radar rainfall estimation may increase. This could partly explain why the performance of the proposed schemes is unstable, in particular, for the EM scheme. Thus, in future work, we will compare or integrate several sources of meteorological data, for instance, from the Meteorological Service of Canada and the National Centers for Environmental Prediction, to maximally decrease the uncertainty induced by the WRF driving data. The second issue is related to the inconsistent spatial scale compared to radar rainfall measurements. Many studies have investigated the inconsistent scale in the comparison of radar and gauge (see section 1). However, as compared to the WRF driving data induced uncertainty, the gauge representativeness error is negligible with the 1 km and 1 hr space-time resolutions used in this study because the spatial variability is relatively small under these scales (Seo & Krajewski, 2010, 2011). The proposed scheme is fully physical based, and the rain gauge is not involved. The other error sources of radar measurement may contaminate the results presented in this study. The weather radar data have been corrected for various sources of radar error including noise, clutter, anomalous propagation, intervening rain attenuation, occultation, range attenuation, bright band, and orographic enhancement. However, processing of radar data is complicated, and it is difficult to address all errors, as well as their interdependences. The goal of this work is to make the proposed scheme one of the essential components in processing radar observational data. The proposed scheme can be employed as the last step in processing raw radar data, after other errors have been minimized. Because the adjustment procedure is highly time consuming, enhancing the efficiency of the scheme could be a key solution to enable its use in real-time applications. We will conduct a series of experiments to improve the model efficiency in future study, such as selecting the optimum spatial and time resolutions to balance the accuracy and efficiency.

In addition, one major assumption of the present work is that a raindrop is independent in the atmosphere, and other microphysical processes such as break up, collision, and coalescence are ignored. It should be noted that evaporation and wind drift are considered as the principle factors that cause discrepancies in radar-gauge rainfall because they lead to changes in the amount of rainfall directly through mass variation and horizontal motion of raindrops. However, other microphysical processes cannot change the rainfall amount directly. However, they can influence wind drift and evaporation by changing the raindrop size distribution. We agree that the change in raindrop size distribution induced by other microphysical processes will bring inevitable uncertainties in the simulation process of evaporation and wind drift. However, they also significantly increase the complexity of the simulation. Thus, this study omits other microphysical processes. We do not expect to accurately simulate all microphysical processes for a raindrop. In fact, there is no need to do so in this work because rainfall is composed of a very large number of integrative raindrops, and the simulated error within a tolerance for a single raindrop will not remarkably affect the final radar rainfall estimation owing to the spatial continuity of rainfall distribution. This work is a pilot study that can raise the research community's attention about the connection between raindrop microphysical processes and radar-gauge rainfall comparison. More significant microphysical processes, such as collision and coalescence, can be included in future studies.

Table 6
Fractional Absolute Difference Between Radar and Gauge Rainfall Measurements for All Events

Event	Original	DM	EM	DEM
1	0.46	0.39	0.47	0.42
2	0.50	0.47	0.47	0.42
3	0.45	0.39	0.45	0.39
4	0.94	0.54	0.79	0.44
5	0.40	0.34	0.37	0.34
6	0.76	0.73	0.62	0.59
7	0.48	0.45	0.44	0.42
8	0.54	0.32	0.46	0.30

Table 7
Hit Ratios (HR) and False Alarm Ratios (FAR) of Radar Rainfall With Gauge Rainfall as Reference for All Events

	HR				*FAR*			
Event	Original	DM	EM	DEM	Original	DM	EM	DEM
1	0.94	0.94	0.94	0.94	0.15	0.14	0.13	0.12
2	0.99	0.99	0.99	0.99	0.21	0.21	0.20	0.20
3	0.91	0.88	0.88	0.88	0.15	0.12	0.15	0.12
4	0.95	0.96	0.95	0.96	0.17	0.15	0.16	0.11
5	0.82	0.82	0.81	0.82	0.10	0.11	0.11	0.11
6	0.93	0.96	0.93	0.94	0.14	0.14	0.13	0.11
7	0.94	0.94	0.94	0.94	0.17	0.17	0.15	0.16
8	0.95	0.95	0.94	0.95	0.08	0.07	0.06	0.06

The selection of ground or three-dimensional atmospheric fields is also worth remarking upon. High spatial and temporal atmospheric fields are needed to simulate microphysical processes associated with the raindrop. The WRF-derived hourly three-dimensional atmospheric fields obtained by downscaling the ECMWF ERA-Interim data, including wind, temperature, pressure, and relative humidity, were used in this work. The possible errors in these estimated fields have been discussed in the literature (Carvalho et al., 2012; Wilson et al., 2011; Zhang et al., 2013). Some ground observations of these fields may have higher accuracy. However, a comparison of the ground wind with the drift direction and distance in Figures 4–6 show that the ground observations cannot replace the three-dimensional atmospheric field in the raindrop evolution simulation. As ECMWF can provide a global reanalysis meteorological data set, the three-dimensional atmospheric fields can be obtained easily in any region of interest, which will significantly reduce the difficulty of applying the proposed method in other areas. Other reanalysis data sets can also be good choices for different climate regimes and research purposes. In summary, it is recommended to use the downscaled three-dimensional atmospheric fields instead of ground observations in related future work.

Lastly, the comparison of radar-gauge rainfall discrepancy under the DM, EM, and DEM adjustments showed different performances for different situations. Among the three adjustment models, none of the models show the best skill at all time steps and locations. This is because the original radar rainfall measurement may suffer to different degrees for raindrop drift and evaporation-induced error. Although uncertainty is associated with the proposed scheme, the adjustment may even agree with the original radar rainfall measurement if the microphysically induced error is not significant. Possible factors affecting the performance of the three models will be investigated in future work. Considering the significant decrease in bias and acceptable improvement in the correlation coefficient, the DEM adjustment appears to be the best scheme, without much loss of generality, at the present time.

6. Conclusion

This study proposes a fully formulated scheme to numerically simulate both the drift and evaporation of raindrops in a three-dimensional atmospheric context and reduces the uncertainties of radar rainfall estimation. The WRF model is used to simulate the high-resolution three-dimensional atmospheric fields, and a dual-polarization radar is adopted to retrieve the raindrop size distribution for each radar pixel. The consistency between the atmospheric observations and the simulated microphysical processes demonstrates the effectiveness of this method. With the ground rainfall from a rain gauge network as reference, the proposed scheme can significantly improve the radar-gauge correlation and reduce the discrepancy for most situations. For event-averaged values over all time steps and locations, the drift (DM), evaporation (EM), and combination scheme (DEM) adjustments can improve the radar-gauge correlation by 3.2%, 2.9%, and 3.8% and reduce their discrepancy by 17.9%, 8.6%, and 21.7%, respectively at most for eight selected events. The combination scheme of DEM has the best performance and is recommended for future radar rainfall quality control.

Some problems remain with the proposed scheme, as discussed in section 5. Some of the problems, such as the start height of a raindrop and DSD retrieval error, have been explored. The evaluation method may also highlight issues with radar-gauge comparisons and create uncertainties such as the point-to-area representative error (Borga et al., 2002) and gauge measurement error. However, this study is a preliminary attempt

at adjusting the impact of both raindrop drift and evaporation on radar-gauge rainfall comparison, which has been alleviated to some extent via the simple scheme proposed in this study and can be easily applied to other study areas. It is acknowledged that a bias correction using rain gauges as a reference is an essential component in all radar rainfall quality control. The inconsistent conditions in comparing radar and gauge rainfall will invariably introduce new uncertainty to the radar rainfall. In future work, a higher number of study areas with diverse climate and geographical conditions will be explored to improve the performance of the proposed method.

Acknowledgments
This work was supported by the National Natural Science Foundation of China (41771424 and 41871299), the Newton Fund via the Natural Environment Research Council (NERC), the Economic and Social Research Council (ESRC) (NE/N012143/1), and the University Natural Science Project of Jiangsu Province (Grant 16KJA170001). The authors acknowledge the British Atmospheric Data Centre and the European Centre for Medium-range Weather Forecasts as the sources of data used in the study. The radar data sets and gauge data sets were sourced from the U.K. Met Office's Nimrod system and the Land and Marine Surface Stations Data (1853–current) of the Met Office Integrated Data Archive System (MIDAS), respectively. Both data sets are available from the NCAS British Atmospheric Data Centre (http://archive.ceda.ac.uk/). The ERA-Interim data driving the WRF model can be downloaded from the ECMWF Public Data sets web interface (https://www.ecmwf.int/).

References

AghaKouchak, A., Bárdossy, A., & Habib, E. (2010). Conditional simulation of remotely sensed rainfall data using a non-Gaussian v-transformed copula. *Advances in Water Resources*, *33*(6), 624–634.

Anagnostou, M. N., Anagnostou, E. N., Vivekanandan, J., & Ogden, F. L. (2008). Comparison of two raindrop size distribution retrieval algorithms for X-band dual polarization observations. *Journal of Hydrometeorology*, *9*(3), 589–600.

Austin, P. M. (1987). Relation between measured radar reflectivity and surface rainfall. *Monthly Weather Review*, *115*(5), 1053–1070.

Berrisford, P., D. Dee, P. Poli, R. Brugge, K. Fielding, M. Fuentes, et al. (2011). The ERA-Interim archive, version 2.0.

Borga, M., Tonelli, F., Moore, R. J., & Andrieu, H. (2002). Long-term assessment of bias adjustment in radar rainfall estimation. *Water Resources Research*, *38*(11), 1226. https://doi.org/10.1029/2001WR000555

Borowska, L., Zrnić, D., Ryzhkov, A., Zhang, P., & Simmer, C. (2011). Polarimetric estimates of a 1-month accumulation of light rain with a 3-cm wavelength radar. *Journal of Hydrometeorology*, *12*(5), 1024–1039.

Brandes, E. A., Zhang, G., & Vivekanandan, J. (2004). Drop size distribution retrieval with polarimetric radar: Model and application. *Journal of Applied Meteorology*, *43*(3), 461–475.

Bringi, V. N., & Chandrasekar, V. (2001). *Polarimetric Doppler weather radar: Principles and applications*. Cambridge: Cambridge University Press.

Bringi, V. N., Chandrasekar, V., Hubbert, J., Gorgucci, E., Randeu, W. L., & Schoenhuber, M. (2003). Raindrop size distribution in different climatic regimes from disdrometer and dual-polarized radar analysis. *Journal of the Atmospheric Sciences*, *60*(2), 354–365.

Bringi, V. N., Huang, G.-J., Chandrasekar, V., & Gorgucci, E. (2002). A methodology for estimating the parameters of a gamma raindrop size distribution model from polarimetric radar data: Application to a squall-line event from the TRMM/Brazil campaign. *Journal of Atmospheric and Oceanic Technology*, *19*(5), 633–645.

Bringi, V. N., Rico-Ramirez, M. A., & Thurai, M. (2011). Rainfall estimation with an operational polarimetric C-band radar in the United Kingdom: Comparison with a gauge network and error analysis. *Journal of Hydrometeorology*, *12*(5), 935–954.

Carvalho, D., Rocha, A., Gómez-Gesteira, M., & Santos, C. (2012). A sensitivity study of the WRF model in wind simulation for an area of high wind energy. *Environmental Modelling and Software*, *33*, 23–34.

Cecinati, F., Rico-Ramirez, M. A., Heuvelink, G. B. M., & Han, D. (2017). Representing radar rainfall uncertainty with ensembles based on a time-variant geostatistical error modelling approach. *Journal of Hydrology*, *548*, 391–405.

Choi, E. (1997). Numerical modelling of gust effect on wind-driven rain. *Journal of Wind Engineering and Industrial Aerodynamics*, *72*, 107–116.

Chow, V. T., Maidment, D. R., & Mays, L. W. (1988). *Applied hydrology*. New York: McGraw-Hill.

Ciach, G. J., Krajewski, W. F., & Villarini, G. (2007). Product-error-driven uncertainty model for probabilistic quantitative precipitation estimation with NEXRAD data. *Journal of Hydrometeorology*, *8*(6), 1325–1347.

Cluckie, I., Griffith, R., Lane, A., & Tilford, K. (2000). Radar hydrometeorology using a vertically pointing radar. *Hydrology*, *4*(4), 565–580.

Collier, C. (1999). The impact of wind drift on the utility of very high spatial resolution radar data over urban areas. *Physics Chemistry of the Earth, Part B: Hydrology, Oceans Atmosphere*, *24*(8), 889–893.

Dai, Q., & Han, D. (2014). Exploration of discrepancy between radar and gauge rainfall estimates driven by wind fields. *Water Resources Research*, *50*, 8571–8588. https://doi.org/10.1002/2014WR015794

Dai, Q., Han, D., Rico-Ramirez, M., & Srivastava, P. K. (2014). Multivariate distributed ensemble generator: A new scheme for ensemble radar precipitation estimation over temperate maritime climate. *Journal of Hydrology*, *511*, 17–27.

Dai, Q., Han, D., Rico-Ramirez, M. A., & Islam, T. (2013). The impact of raindrop drift in a three-dimensional wind field on a radar–gauge rainfall comparison. *International Journal of Remote Sensing*, *34*(21), 7739–7760.

Dai, Q., Rico-Ramirez, M. A., Han, D., Islam, T., & Liguori, S. (2015). Probabilistic radar rainfall nowcasts using empirical and theoretical uncertainty models. *Hydrological Processes*, *29*(1), 66–79.

Dee, D. P., Uppala, S. M., Simmons, A. J., Berrisford, P., Poli, P., Kobayashi, S., et al. (2011). The ERA-Interim reanalysis: Configuration and performance of the data assimilation system. *Quarterly Journal of the Royal Meteorological Society*, *137*(656), 553–597. https://doi.org/10.1002/qj.828

Dudhia, J. (1989). Numerical study of convection observed during the winter monsoon experiment using a mesoscale two-dimensional model. *Journal of the Atmospheric Sciences*, *46*(20), 3077–3107.

Feingold, G., & Levin, Z. (1986). The lognormal fit to raindrop spectra from frontal convective clouds in Israel. *Journal of Climate and Applied Meteorology*, *25*(10), 1346–1363.

Frasier, S. J., Kabeche, F., Ventura, J. F. I., Al-Sakka, H., Tabary, P., Beck, J., & Bousquet, O. (2013). In-place estimation of wet radome attenuation at X band. *Journal of Atmospheric and Oceanic Technology*, *30*(5), 917–928.

Germann, U., Berenguer, M., Sempere-Torres, D., & Zappa, M. (2009). REAL—Ensemble radar precipitation estimation for hydrology in a mountainous region. *Quarterly Journal of the Royal Meteorological Society*, *135*(639), 445–456.

Golding, B. (1998). Nimrod: A system for generating automated very short range forecasts. *Meteorological Applications*, *5*(1), 1–16.

Gorgucci, E., Chandrasekar, V., Bringi, V., & Scarchilli, G. (2002). Estimation of raindrop size distribution parameters from polarimetric radar measurements. *Journal of the Atmospheric Sciences*, *59*(15), 2373–2384.

Gorgucci, E., Scarchilli, G., Chandrasekar, V., & Bringi, V. (2000). Measurement of mean raindrop shape from polarimetric radar observations. *Journal of the Atmospheric Sciences*, *57*(20), 3406–3413.

Gourley, J. J., Illingworth, A. J., & Tabary, P. (2009). Absolute calibration of radar reflectivity using redundancy of the polarization observations and implied constraints on drop shapes. *Journal of Atmospheric and Oceanic Technology*, *26*(4), 689–703.

Habib, E., Aduvala, A. V., & Meselhe, E. A. (2008). Analysis of radar-rainfall error characteristics and implications for streamflow simulation uncertainty. *Hydrological Sciences Journal*, *53*(3), 568–587.
Harrison, D., K. Norman, T. Darlington, D. Adams, N. Husnoo, C. Sandford, and S. Best (2015). The evolution of the Met Office radar data quality control and product generation system: Radarnet, paper presented at Proceedings of the 37th AMS Conference on Radar Meteorology, Norman, OK, USA.
Hasan, M. M., Sharma, A., Mariethoz, G., Johnson, F., & Seed, A. (2016). Improving radar rainfall estimation by merging point rainfall measurements within a model combination framework. *Advances in Water Resources*, *97*, 205–218.
Islam, T., Rico-Ramirez, M. A., Thurai, M., & Han, D. (2012). Characteristics of raindrop spectra as normalized gamma distribution from a Joss–Waldvogel disdrometer. *Atmospheric Research*, *108*, 57–73.
Janjić, Z. I. (1994). The step-mountain eta coordinate model: Further developments of the convection, viscous sublayer, and turbulence closure schemes. *Monthly Weather Review*, *122*(5), 927–945.
Kain, J. S. (2004). The Kain–Fritsch convective parameterization: an update. *Journal of Applied Meteorology*, *43*(1), 170–181.
Kim, D., Maki, M., & Lee, D. (2010). Retrieval of three-dimensional raindrop size distribution using X-band polarimetric radar data. *Journal of Atmospheric and Oceanic Technology*, *27*(8), 1265–1285.
Kumjian, M. R., & Ryzhkov, A. V. (2010). The impact of evaporation on polarimetric characteristics of rain: Theoretical model and practical implications. *Journal of Applied Meteorology and Climatology*, *49*(6), 1247–1267.
Kurri, M., & Huuskonen, A. (2008). Measurements of the transmission loss of a radome at different rain intensities. *Journal of Atmospheric and Oceanic Technology*, *25*(9), 1590–1599.
Lack, S. A., & Fox, N. I. (2007). An examination of the effect of wind-drift on radar-derived surface rainfall estimations. *Atmospheric Research*, *85*(2), 217–229.
Lang, T. J., Nesbitt, S. W., & Carey, L. D. (2009). On the correction of partial beam blockage in polarimetric radar data. *Journal of Atmospheric and Oceanic Technology*, *26*(5), 943–957.
Lauri, T., Koistinen, J., & Moisseev, D. (2012). Advection-based adjustment of radar measurements. *Monthly Weather Review*, *140*(3), 1014–1022.
Li, X., & Srivastava, R. C. (2001). An analytical solution for raindrop evaporation and its application to radar rainfall measurements. *Journal of Applied Meteorology*, *40*(9), 1607–1616.
Met-Office (2012). Met Office Integrated Data Archive System (MIDAS) land and marine surface stations data (1853–current), edited, NCAS British Atmospheric Data Centre.
Met-Office (2014). Hameldon Hill C-band rain radar dual polar products. NCAS British Atmospheric Data Centre, edited.
Mittermaier, M. P., Hogan, R. J., & Illingworth, A. J. (2004). Using mesoscale model winds for correcting wind-drift errors in radar estimates of surface rainfall. *Quarterly Journal of the Royal Meteorological Society*, *130*(601), 2105–2123.
Mlawer, E. J., Taubman, S. J., Brown, P. D., Iacono, M. J., & Clough, S. A. (1997). Radiative transfer for inhomogeneous atmospheres: RRTM, a validated correlated-k model for the longwave. *Journal of Geophysical Research*, *102*(D14), 16,663–16,682.
Nerini, D., Besic, N., Sideris, I., Germann, U., Foresti, L. J. H., & Sciences, E. S. (2017). A non-stationary stochastic ensemble generator for radar rainfall fields based on the short-space Fourier transform. *Hydrology and Earth System Sciences*, *21*(6), 2777–2797.
Niu, G.-Y., Yang, Z. L., Mitchell, K. E., Chen, F., Ek, M. B., Barlage, M., et al. (2011). The community Noah land surface model with multiparameterization options (Noah-MP): 1. Model description and evaluation with local-scale measurements. *Journal of Geophysical Research*, *116*, D12109. https://doi.org/10.1029/2010JD015139
Pallardy, Q., & Fox, N. I. (2018). Accounting for rainfall evaporation using dual-polarization radar and mesoscale model data. *Journal of Hydrology*, *557*, 573–588.
Park, S., Maki, M., Iwanami, K., Bringi, V., & Chandrasekar, V. (2005). Correction of radar reflectivity and differential reflectivity for rain attenuation at X band. Part II: Evaluation and application. *Journal of Atmospheric and Oceanic Technology*, *22*(11), 1633–1655.
Powers, J. G., Klemp, J. B., Skamarock, W. C., Davis, C. A., Dudhia, J., Gill, D. O., et al. (2017). The Weather Research and Forecasting Model: Overview, system efforts, and future directions. *Bulletin of the American Meteorological Society*, *98*(8), 1717–1737. https://doi.org/10.1175/BAMS-D-15-00308.1
Rogers, R., & Yau, M. K. (1996). *A short course in cloud physics*. Oxford: Elsevier.
Rosenfeld, D., & Mintz, Y. (1988). Evaporation of rain falling from convective clouds as derived from radar measurements. *Journal of Applied Meteorology*, *27*(3), 209–215.
Seo, B.-C., & Krajewski, W. F. (2010). Scale dependence of radar rainfall uncertainty: Initial evaluation of NEXRAD's new super-resolution data for hydrologic applications. *Journal of Hydrometeorology*, *11*(5), 1191–1198.
Seo, B.-C., & Krajewski, W. F. (2011). Investigation of the scale-dependent variability of radar-rainfall and rain gauge error covariance. *Advances in Water Resources*, *34*(1), 152–163.
Song, Y., Han, D., & Zhang, J. (2017). Radar and rain gauge rainfall discrepancies driven by changes in atmospheric conditions. *Geophysical Research Letters*, *44*, 7303–7309. https://doi.org/10.1002/2017GL074493
Testik, F., & Pei, B. (2017). Wind effects on the shape of raindrop size distribution. *Journal of Hydrometeorology*, *18*(5), 1285–1303.
Testik, F., & Rahman, M. (2016). High-speed optical disdrometer for rainfall microphysical observations. *Journal of Atmospheric and Oceanic Technology*, *33*(2), 231–243.
Testik, F., & Rahman, M. (2017). First in situ observations of binary raindrop collisions. *Geophysical Research Letters*, *44*, 1175–1181. https://doi.org/10.1002/2017GL072516
Testud, J., Oury, S., Black, R. A., Amayenc, P., & Dou, X. (2001). The concept of "normalized" distribution to describe raindrop spectra: A tool for cloud physics and cloud remote sensing. *Journal of Applied Meteorology*, *40*(6), 1118–1140.
Thompson, G., & Eidhammer, T. (2014). A study of aerosol impacts on clouds and precipitation development in a large winter cyclone. *Journal of the Atmospheric Sciences*, *71*(10), 3636–3658.
Thorndahl, S., Nielsen, J. E., & Rasmussen, M. R. (2014). Bias adjustment and advection interpolation of long-term high resolution radar rainfall series. *Journal of Hydrology*, *508*, 214–226.
Ulbrich, C. W. (1983). Natural variations in the analytical form of the raindrop size distribution. *Journal of Climate and Applied Meteorology*, *22*(10), 1764–1775.
Villarini, G., & Krajewski, W. F. (2010). Review of the different sources of uncertainty in single polarization radar-based estimates of rainfall. *Surveys in Geophysics*, *31*(1), 107–129.
Villarini, G., Seo, B.-C., Serinaldi, F., & Krajewski, W. F. (2014). Spatial and temporal modeling of radar rainfall uncertainties. *Atmospheric Research*, *135-136*, 91–101.

Wilson, A. B., Bromwich, D. H., & Hines, K. M. (2011). Evaluation of Polar WRF forecasts on the Arctic System Reanalysis domain: Surface and upper air analysis. *Journal of Geophysical Research*, *116*, D11112. https://doi.org/10.1029/2010JD015013

Xie, X., Evaristo, R., Troemel, S., Saavedra, P., Simmer, C., & Ryzhkov, A. (2016). Radar observation of evaporation and implications for quantitative precipitation and cooling rate estimation. *Journal of Atmospheric and Oceanic Technology*, *33*(8), 1779–1792.

Zhang, H., Pu, Z., & Zhang, X. (2013). Examination of errors in near-surface temperature and wind from WRF numerical simulations in regions of complex terrain. *Weather and Forecasting*, *28*(3), 893–914.